

Strained Pt(221) Facet in a PtCo@Pt-Rich Catalyst Boosts Oxygen Reduction and Hydrogen Evolution Activity

Emmanuel Batsa Tetteh,^{II} Caleb Gyan-Barimah,^{II} Ha-Young Lee,^{II} Tong-Hyun Kang, Seonghyeon Kang, Stefan Ringe,* and Jong-Sung Yu*



Cite This: *ACS Appl. Mater. Interfaces* 2022, 14, 25246–25256



Read Online

ACCESS |

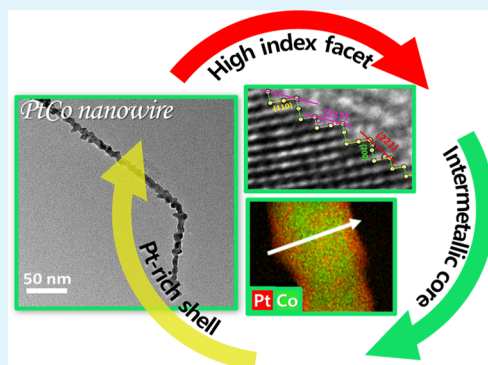
Metrics & More

Article Recommendations

Supporting Information

ABSTRACT: Over the last years, the development of highly active and durable Pt-based electrocatalysts has been identified as the main target for a large-scale industrial application of fuel cells. In this work, we make a significant step ahead in this direction by preparing a high-performance electrocatalyst and suggesting new structure–activity design concepts which could shape the future of oxygen reduction reaction (ORR) catalyst design. For this, we present a new one-dimensional nanowire catalyst consisting of a L₁₀ ordered intermetallic PtCo alloy core and compressively strained high-index facets in the Pt-rich shell. We find the nanoscale PtCo catalyst to provide an excellent turnover for the ORR and hydrogen evolution reaction (HER), which we explain from high-resolution transmission electron microscopy and density functional theory calculations to be due to the high ratio of Pt(221) facets. These facets include highly active ORR and HER sites surprisingly on the terraces which are activated by a combination of sub-surface Co-induced high Miller index-related strain and oxygen coverage on the step sites. The low dimensionality of the catalyst provides a cost-efficient use of Pt. In addition, the high catalytic activity and durability are found during both half-cell and proton exchange membrane fuel cell (PEMFC) operations for both ORR and HER. We believe the revealed design concepts for generating active sites on the Pt-based catalyst can open up a new pathway toward the development of high-performance cathode catalysts for PEMFCs and other catalytic systems.

KEYWORDS: intermetallic, nanowire, PEMFC, high-index facets, HER, density functional theory



1. INTRODUCTION

The transportation industry accounts for a quarter of the world's energy consumption creating an increased demand for clean and energy efficient forms of transport.¹ Proton exchange membrane fuel cells (PEMFCs) which convert the chemical energy of hydrogen into electricity show great potential as power sources for automobiles; hence, several automotive manufacturers have begun the commercialization of fuel cell electric vehicles.² However, the current PEMFC catalyst which is based on expensive Pt nanoparticles (NPs) supported on carbon hinders the wide spread application of PEMFCs.^{3,4} Lowering the Pt loading in the fuel cell to a sustainable level is necessary for the wide deployment of PEMFC. This is attained through alloying with cheaper metals.⁵

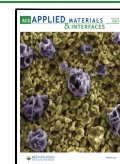
The Pt–Co alloy system has been long studied due to its unique properties with potential application toward many electrocatalytic energy conversion reactions.^{6–9} Earlier work by Stamenkovic and co-workers presented a typical case where Pt₃Co among different Pt₃M (M = Ni, Co, Fe, Ti, V) alloys distinguished itself with a good balance between the adsorption energies of intermediates and the surface coverage by spectator species during oxygen reduction reaction (ORR), hence positioning it on top of the volcano plot of catalytic

activity as a function of the d-band center.¹⁰ Unsurprisingly, the Pt–Co alloy is currently the commercialized catalyst for the Toyota MIRAI fuel cell vehicle.² Theoretical studies predicted that alloying Pt with Co could result in an optimal adsorption energy for oxygen species leading to highly active ORR catalysts.^{10,11} These predictions have been confirmed by a number of experimental studies.^{12–14} The observed activity enhancements mainly arose from the ligand and strain effect which is realized by the judicious tuning of the near-surface composition of the catalyst.^{7,15–17} Engineering the shape of the catalyst to selectively expose a specific arrangement of surface atoms can leverage the facet effect and provide an avenue to tune the performance of active sites.^{18–20} Fundamental studies on crystalline surfaces have demonstrated that high-index facets show much higher catalytic activity than low-index planes because of their greater density of unsaturated atomic

Received: January 7, 2022

Accepted: May 11, 2022

Published: May 24, 2022



steps, ledges, and kinks serving as active sites for breaking chemical bonds.^{21–23} Many researchers have reported different ways to synthesize such high-indexed facet bounded catalytic materials. A combination of these multiple activity enhancement strategies in a single Pt–Co alloy catalyst can yield a high-performance catalyst with the potential for industrial application. Despite these important insights, systematic design concepts about these complex materials are still missing until today, mainly due to a lack of knowledge about the actual active site for ORR.

In addition, the stability of the Pt–Co alloy system has always been seen as unsatisfactory and numerous research efforts have consequently been devoted to the improvement of stability and durability.^{24–26} Several factors can reduce the lifetime of carbon-supported Pt–Co electrocatalysts including Co dissolution and carbon support corrosion.^{27–30} Typically, the Pt–Co alloys adopt a face-centered cubic (fcc) structure in the form of disordered solid solutions, in which the Pt and Co atoms are randomly distributed. De-alloying can easily occur under the highly corrosive PEMFC condition, resulting in compromised performance. Atomically ordering the alloy structure is one approach to improve the alloy stability.^{31–33} Sun and co-workers reported a class of atomically ordered L₁₀ CoPt intermetallic NPs.³⁴ Unlike the fcc L₁₂ intermetallic Pt–Co with ratio near 3:1, the tetragonal L₁₀-intermetallic Pt–Co with the near 1:1 ratio resulted in a stronger coupling of the Co (3d) and Pt (5d) atomic orbitals along the crystallographic *c* direction than the cubic counterpart, improving the stability of Co against electrochemical and chemical etching. Another stabilizing approach is to employ a Pt shell coating on the alloy (core–shell structure).^{14,35–37} These two strategies can prevent the loss of the alloying element. However, a critical degradation path for the loss of electrochemical surface area (ECSA) in a carbon-supported Pt-based catalyst has been attributed to the detachment and migration of the Pt NPs from the carbon support followed by coalescence and aggregation.^{24,38} One-dimensional (1D) structures in the form of nanowires (NWs) provide immunity to particle detachment, migration, and coalescence because of the large contact area for anchoring the metal on the support.³⁹ Although larger diameter NWs are more stable, they yield limited Pt utilization. Too thin NWs nevertheless compromise durability.⁴⁰ As mentioned by Bu et al., there is always a trade-off between Pt utilization and durability when using 1D Pt structures for ORR.⁹

Taking motivation from the previous progress in this field, we herein report a Pt–Co-based PtCo@Pt core–shell electrocatalyst endowed with a highly active catalytic surface arising from strain effects on the high-index Pt(221) facet. We also incorporated the necessary structural features required for enhanced durability which includes an ordered sub-surface intermetallic alloy core, a thick Pt shell, and a larger Pt–carbon contact area. Interestingly, the catalyst showed excellent performance for both ORR and hydrogen evolution reaction (HER) under acidic and alkaline conditions, as well as high durability. Using a combination of high-resolution transmission electron microscopy (HR-TEM) and density functional theory (DFT) calculations, we were further able to reveal the ORR active site for this material and the structural activation mechanism which opens up new windows for the design of novel ORR electrocatalysts.

2. EXPERIMENTAL DETAILS

2.1. Materials and Chemicals. All reagents were of analytical grade and were used as received without further purification. Platinum(II) acetylacetone [Pt(acac)₂, 98%], cobalt(III) acetylacetone [Co(acac)₃, 99.99%], cetyltrimethylammonium chloride (CTAC, 99.0%), glucose (C₆H₁₂O₆, ≥99.5%), benzoic acid (C₆H₅COOH, ≥99.5%), phloroglucinol (C₆H₆O₃ ≥ 99.0%), ascorbic acid (AA), sodium borohydride (NaBH₄ ≥ 98.0%), chromium (0) hexacarbonyl (Cr(CO)₆ ≥ 98%), 1-octadecene (ODE, 90%), and oleylamine (OAm, 70%) were purchased from Sigma-Aldrich. Commercial Pt/C [19.4 wt % Pt, Tanaka Kikinzoku Kogyo (TKK), Japan] was purchased from Tanaka Kikinzoku Kogyo, Japan, and commercial carbon (Vulcan XC72) from Cabot. *N,N*-Dimethylformamide (DMF, 99.9%) and ethylene glycol (99.9%) were purchased from Samchun Chemical. The water used in all experiments was made by passing through an ultrapure purification system.

2.2. Synthesis of Catalysts. **2.2.1. Preparation of PtCo NW.** In a typical synthesis, 0.26 mmol Pt(acac)₂, 0.28 mmol Co(acac)₃, 1.8 mmol CTAC, 1.6 mmol glucose, 20 mL of OAm, and 20 mL of ODE were added into a three-necked flask equipped with a stirrer. The reaction mixture was degassed at 120 °C for 20 min under vacuum and further heated to 250 °C under a nitrogen blanket at 5 °C/min then held at 250 °C for 30 min for the growth of the NWs. The reaction was stopped by removing the heating source and allowing to cool down to room temperature. The reaction product was then centrifuged with added ethanol and toluene. The black product was then dispersed in toluene and mixed with Vulcan carbon initially dispersed in ethanol with a targeted metal loading of 20 wt %. After sonication for 10 min, the resulting product was collected by vacuum filtration and dried. Subsequently, high-temperature heat treatment was performed in 5% H₂/Ar mixture gas at 550 °C.

2.2.2. Preparation of PtCo NP. PtCo NPs were prepared by a protocol modified from one previously reported.²⁷ In a typical synthesis, 0.04 mmol Pt(acac)₂, 0.05 mmol Co(acac)₃, 0.74 mmol benzoic acid, and 30 mg of commercial Vulcan carbon dispersed in 15 mL of DMF were added into a vial (volume: 50 mL). After the vial was capped, the mixture was ultra-sonicated for 20 min. The resulting homogeneous mixture was then heated from room temperature and maintained at 160 °C for 12 h under stirring in an oil bath before it was cooled to room temperature. The resulting colloidal product was collected by centrifugation and washed three times with an ethanol/acetone mixture. The black product was then collected by vacuum filtration and dried. Subsequently, heat treatment was performed in 5% H₂/Ar at 300 °C, and the final product was collected for further characterization.

2.3. Physicochemical Characterization. The synthesized catalysts were characterized by powder X-ray diffraction (XRD), X-ray photoelectron spectroscopy (XPS), transmission electron microscopy (TEM) and HR-TEM, energy-dispersive X-ray spectroscopy (EDS), and inductively coupled plasma–optical emission spectrometry. Details are supplied in the [Supporting Information](#).

2.4. Electrochemical Characterization. Electrochemical tests were carried out at room temperature in a three-electrode cell using a rotating disk electrode (RDE) connected to an electrochemical analyzer (Biologic VMP3). Detailed methods are supplied in the [Supporting Information](#).

2.5. Fuel Cell MEA Test. The fuel cell performance of individual PtCo/C NW and PtCo/C NP as well as commercial Pt/C (19.4 wt % Pt, TKK) as a cathode catalyst was tested at a single cell system using the gas diffusion electrode with an active area of 10 cm². The polarization curve was recorded using a PEMFC test station (Scitech Inc., KOREA) with an electronic load (PLZ664WA, Kikusui). Detailed methods are supplied in the [Supporting Information](#).

2.6. Computational Calculations. All DFT calculations of reaction energetics were carried out with a periodic plane-wave implementation and projector augmented wave pseudopotentials using VASP 5.4.4, interfaced with the atomistic simulation environment and the detailed methods are supplied in the [Supporting Information](#).

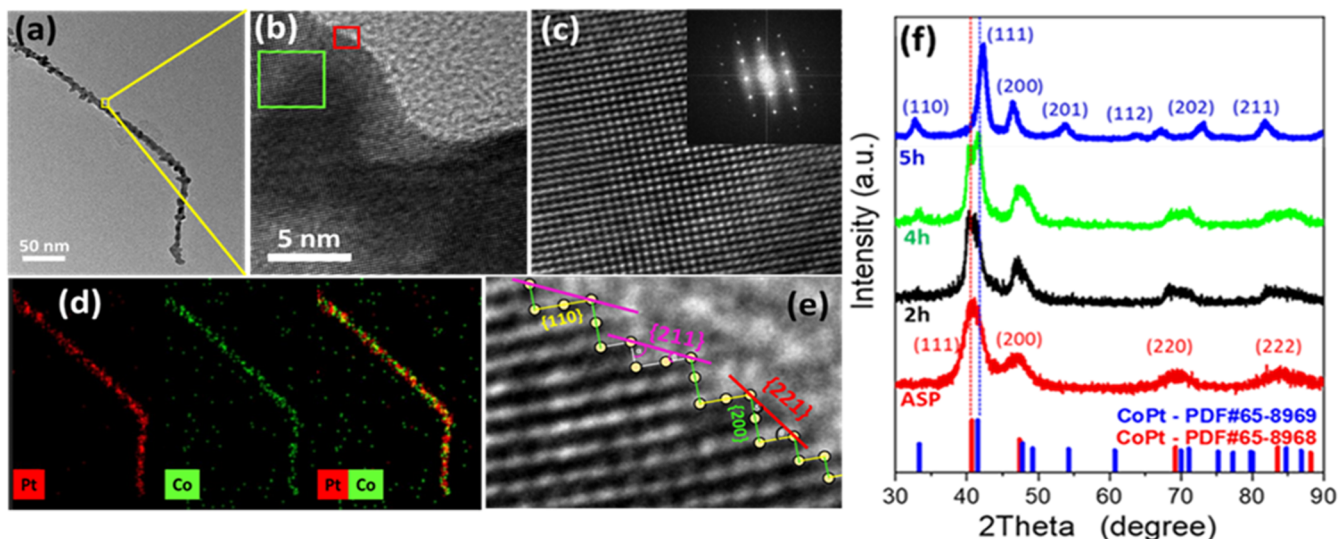


Figure 1. (a) TEM image of PtCo/C NW annealed at 550 °C (b) corresponding HR-TEM image, (c) HR-TEM image and insert represents FFT of green marked region in (b,d) EDS elemental mapping, and (e) HR-TEM image of red marked region in (b,f) XRD spectra of PtCo/C NW before annealing (ASP) and after subsequent hours of annealing at 550 °C (2, 4, and 5 h).

3. RESULTS AND DISCUSSION

3.1. Catalyst Synthesis and Characterization. The high-index faceted PtCo@Pt-rich core–shell alloy NWs (Figure 1a,e) hereafter referred to as PtCo NW were prepared by a facile wet-chemical approach in which platinum(II) acetylacetone, Pt(acac)₂, and cobalt(III) acetylacetone, Co(acac)₃, were simultaneously reduced in a mixture solvent of ODE and OAm. In contrast to previous reports of the synthesis of similar 1D nanostructures in a single solvent OAm system,^{9,41,42} a combination of ODE and OAm was necessary for the generation of 1D nanostructures in our synthetic protocol, and no product was collected after the reaction when only ODE was used as solvent. Depending on the OAm/ODE ratio, different morphologies are obtained, and the 1D shape begins to form with an OAm/ODE volume ratio of 1:0.5 and an optimum ratio of 1:1 yielded the full NWs (Figure S1 in the Supporting Information).

We confirmed the reproducibility of our synthesis method and considered other factors that affect the morphology of the prepared products (Figures S2–S7). We found that the presence of both glucose and CTAC was necessary for the formation of NWs and typical synthesis with all other parameters the same as described except the absence of glucose or CTAC resulted in non 1D nanostructures (Figures S3 and S4). Increasing the amount of either glucose or CTAC did not significantly affect the shape of the wires, but a higher amount of glucose or CTAC required more wash cycles. When we replaced CTAC with CTAB, we observed that the NWs possessed a slightly smoother surface structure (Figure S5) which indicates that the choice of halide plays a role in the formation of the high-index facets. We considered various reducing agents (NaBH₄, metal carbonyl, phloroglucinol, and AA) and the corresponding TEM images (Figure S6) indicate the formation of a non 1D structure. AA as a reducing agent yielded no products. We also considered other solvents and solvent mixtures and the corresponding TEM analysis (Figure S7) revealed the effect of the choice of solvent. The morphologies of the prepared NWs were initially characterized by transmission electron microscopy (TEM) (Figure S8) before loading onto the carbon support. The PtCo NWs have

an irregular surface along the whole length with the diameter on average estimated to be ~15 nm and a length of several hundred nm. XRD patterns of the as-prepared (ASP) PtCo NWs present the fcc phase, and the three main diffraction peaks (111), (200), and (220) are located between those for Pt and Co (Figure 1f). For comparison, PtCo NPs were also synthesized following a previously reported protocol. The PtCo NPs dispersed on a Vulcan carbon support (Figure S9) also displayed similar diffraction pattern (Figure S10) with no detectable impurity peaks of pure Pt and pure Co. This indicates that only a single PtCo phase exists in the as-prepared samples. Subsequently, controlled thermal annealing in a reducing gas atmosphere (5% H₂/Ar) at 550 °C transformed the carbon-supported NWs from fcc to the ordered L1₀ face-centered tetragonal (fct) intermetallic structure (Figure 1f).

The TEM and HR-TEM images of the annealed NWs (Figures 1a and S11) reveal that they maintain their initial morphology. This makes them unique because they require no protective coating against sintering at the high annealing temperature. Similar thermal annealing protocol was applied to the PtCo/C NPs for the phase transformation. Although the phase transformation was successful (Figure S12), the annealing resulted in severe sintering and agglomeration (Figure S13), indicating that the 1D structure is the reason for the high thermal stability.⁹ The phase transformation process of the PtCo/C NW from the fcc to the fct was traced by recording the XRD spectra (Figure 1f) after successive times of heat treatment. Each treatment time gradually transformed the alloy phase of the NWs, evidenced with the corresponding appearance of the (110) superstructure peak at 2θ value of 33.4° and also the shift of the (111) diffraction peak to higher angles, which are characteristic of the L1₀ structure. The HR-TEM image in Figure 1b shows a blow-up of the annealed NW. The green square marked region of Figure 1b is shown in Figure 1c with corresponding fast Fourier transform (FFT) insert, revealing the high crystallinity of the annealed NW. The red square marked region of Figure 1b is blown up in Figure 1e to show the edge of the annealed NW. The edges of the annealed NW (Figures 1e and S14b) possess the high-index facets (221), (211), and (311) as shown

by the inter-planer distances and the stepped atomic terminations (Figure S14). EDS elemental mapping shows the homogeneity in Co distribution throughout a NW before (Figure S15) and after (Figure 1d) annealing. Interestingly, the mapping after annealing shows that the Pt map has a slightly larger area than the Co map, suggesting a Pt-rich layer on the surface of the NWs. The elemental percentage ratio of Pt/Co as measured from the EDX spectra is 50.19/49.81 for the PtCo/C NW and 48.80/51.20 for the PtCo/C NP (Figure S16).

The surface composition and valence states of elements in the annealed PtCo/C NW and PtCo/C NP were analyzed by XPS and compared to those of commercial Pt/C (Figure 2).

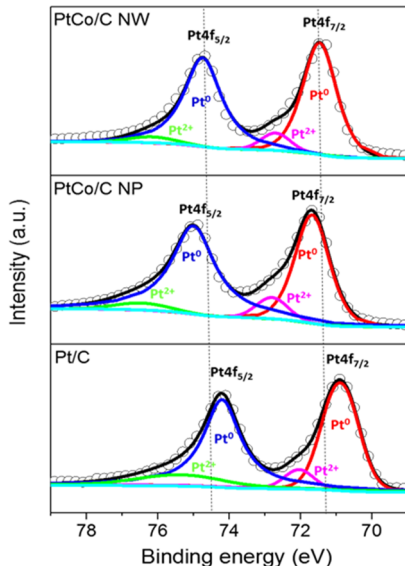


Figure 2. High-resolution Pt 4f XPS spectra of PtCo/C NW, PtCo/C NP, and Pt/C.

The survey spectra for both the PtCo/C NW and PtCo/C NP indicate the coexistence of Pt and Co in the catalyst (Figure S17) from which the surface atomic ratio was determined. Surface-sensitive XPS with shallow detection depth of ~10 nm shows that the PtCo/C NW possesses a Pt-rich shell (Pt at. % > 90), while the PtCo/C NP has a regular alloy shell (66.71/33.29 for Pt/Co).

The deconvoluted Pt 4f XPS spectra for all the samples (PtCo/C NW, PtCo/C NP, and Pt/C) are illustrated in Figure 2. They display the typical $4f_{7/2}$ and $4f_{5/2}$ Pt doublets. Specifically, the $Pt^0\ 4f_{7/2}$ peak is located at binding energies of 71.46, 71.67, and 70.89 eV for PtCo/C NW, PtCo/C NP and Pt/C, respectively. Both doublets of the PtCo alloys are shifted to higher binding energies relative to pure Pt. It is known that for the late transition metals (elements in the right side of the d-block of the periodic table; thus group 8 to 11), the variation in surface core-level shifts for metal overlayers is rather accompanied by a similar shift in the center of the d bands, while charge transfer effects based on electronegativity are inadequate for explaining the shifts.⁴³ For this reason, we attribute the forward shift in binding energies of both PtCo alloys to an increase in Pt d-band vacancy. The shift is more significant for PtCo/C NP due to the higher atomic content of alloying cobalt in the near-surface region. This observation is also confirmed by the Co 2p XPS spectra (Figure S18). The higher affinity for oxygen by the near surface cobalt affected

the degree of surface oxidation in both alloy catalyst as revealed by the percentage composition of Pt^0 to Pt^{2+} from the deconvoluted Pt 4f XPS spectra. The (Pt^0/Pt^{2+}) ratios for PtCo/C NW and PtCo/C NP are 90/10 and 86/14, respectively.

High-resolution scanning TEM (STEM)-EDS mapping and line scan further confirm the core–shell nature of the NW, revealing a 1:1 PtCo core with a thick Pt-rich shell of about 2 nm on the surface of the annealed NWs (Figure 3), which is in

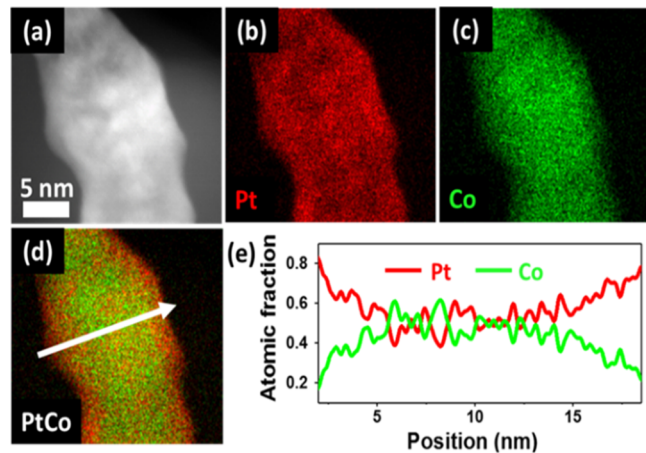


Figure 3. (a) High-resolution STEM image, (b–d) STEM-EDS mapping images of a PtCo/C NW, indicating Pt, Co, and the combination and (e) corresponding line scan profile.

good agreement with the XPS result. Considering that the percentage of Co on the catalyst surface as revealed by XPS analysis is less than 10% even though the penetration depth of XPS is more than 2 nm and the steep composition gradient of Co from the core to the surface, we conclude that there is no Co in the surface layer of the catalyst and even if such Co atom exist in the surface, it would be leached out owing to the harsh conditions of the PEMFC cathode. For this reason, we adopted the conventional PtCo@Pt naming and classify our catalyst as a core–shell type material. We reiterate that there exists a pure Pt surface layer on top of a 2 nm thick Pt-rich shell covering a PtCo core.

3.2. Catalytic Activity and Durability for ORR in Liquid Half-Cell. The PtCo/C NW was analyzed as a catalyst for ORR by employing the RDE method in 0.1 M $HClO_4$ and compared to PtCo/C NP annealed in 5% H_2/Ar at 300 °C and commercial Pt/C. The cyclic voltammograms (CVs) of the catalysts were performed in an N_2 -saturated 0.1 M $HClO_4$ solution at a sweep rate of 50 mV/s at room temperature. From the charge of hydrogen desorption, the ECSA of each catalyst was calculated to be 31, 45, and 65 m^2/g_{Pt} for PtCo/C NW, PtCo/C NP, and Pt/C catalysts, respectively. Figure 4a shows the ORR polarization curves of all the catalysts normalized by the geometric area ($0.196\ cm^2$) of the 5 mm glassy carbon current collector. All electrodes were pre-treated by cycling the potential between 0.05 and 1.10 V versus RHE at a sweep rate of 50 mV/s for several cycles until stable CVs were achieved. The half-wave potential ($E_{1/2}$) for the PtCo/C NWs and PtCo/C NPs were considerably higher than that of the commercial Pt/C catalyst, suggesting the excellent ORR activity of the PtCo alloys.

The kinetic currents of all the catalysts (Figure 4b) were calculated by considering the mass-transport correction using

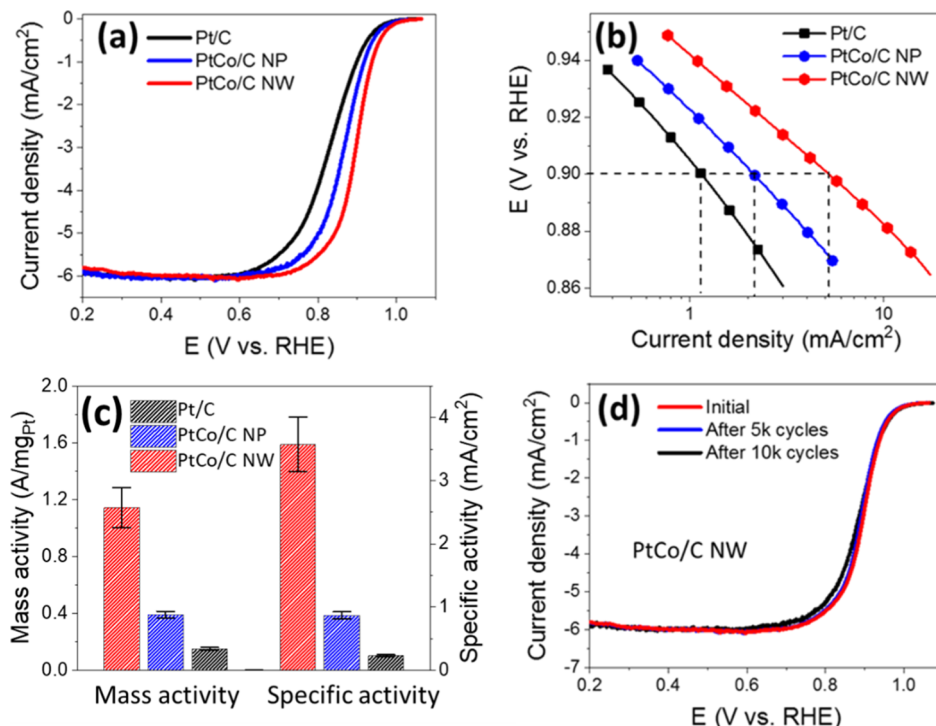


Figure 4. Electrochemical performance. (a) ORR polarization curves, (b) kinetic currents, and (c) histogram of mass activity (MA) and specific activity (SA) of the PtCo/C NW, PtCo/C NP, and commercial Pt/C. (d) ORR polarization curves of PtCo/C NW before and after 5k and 10k potential cycles.

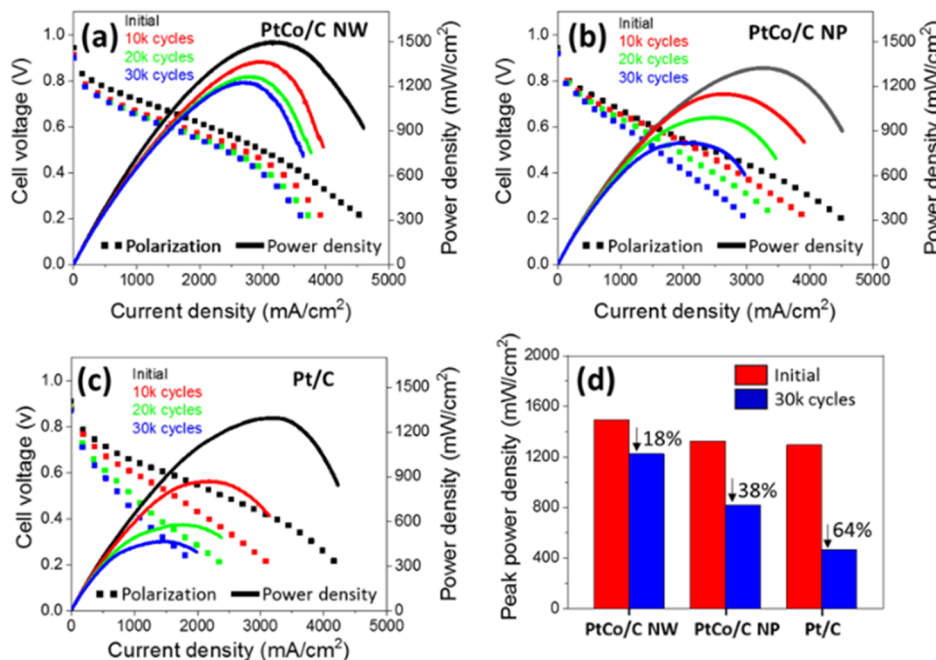


Figure 5. PEMFC MEA polarization curves obtained with H₂/O₂ feed for (a) PtCo NW cathode MEA, (b) PtCo NP cathode MEA, and (c) Pt/C cathode MEA. (d) Histogram of peak power densities of different electrocatalysts before and after ADT for 30,000 cycling.

the Koutecky–Levich equation. The MA and SAs (Figure 4c) were then derived by normalizing the kinetic current by the mass loading of Pt and the ECSA of the catalyst, respectively. In all, the PtCo/C NW showed a MA of 1.30 A/mg_{Pt} at 0.90 V versus RHE, far higher than 0.42 A/mg_{Pt} for the PtCo/C NP catalyst and 0.14 A/mg_{Pt} for the commercial Pt/C catalyst, indicating about 9 times higher MA for PtCo/C NW relative to that of commercial Pt/C. Comparing this performance with

other Pt–Co alloy systems reported in the literature for the ORR under similar conditions, it was confirmed that this PtCo/C NW catalyst exhibits one of the highest electrocatalytic activities for the ORR (Table S1), 3 times higher than the 2020–2025 target set by the U.S. Department of Energy (DOE) (0.44 A/mg_{Pt} at 0.90 V).⁴⁴ In addition to the higher SA and MAs, the PtCo/C NW exhibited remarkable durability during the accelerated degradation test (ADT). The durability

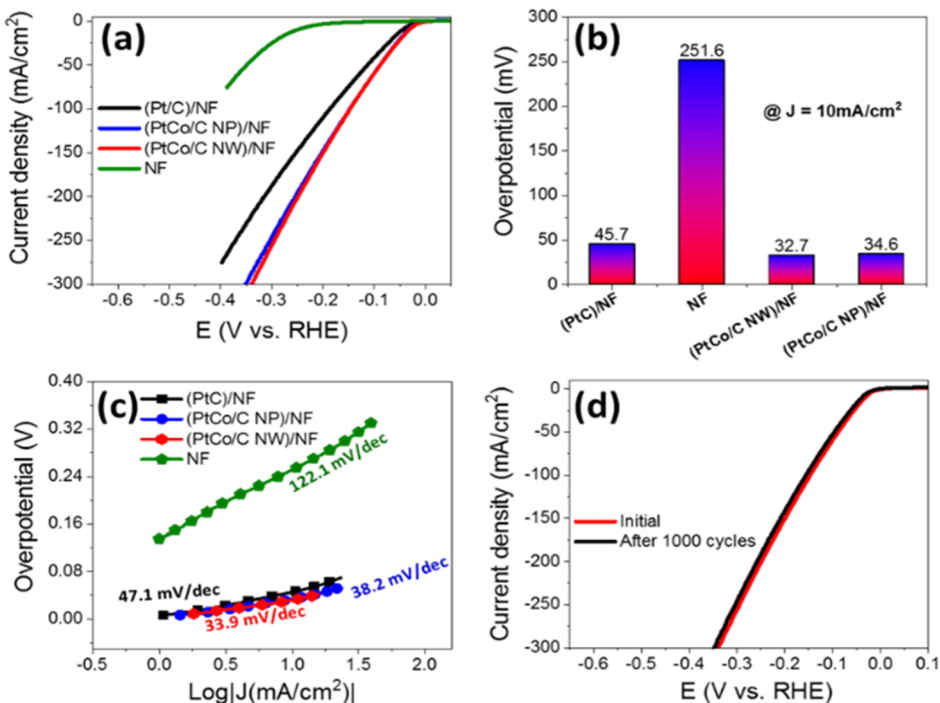


Figure 6. Catalytic performance for HER. (a) HER polarization curves, (b) histogram of overpotentials at a current density of $10 \text{ mA}/\text{cm}^2$ in 1.0 M KOH , and (c) Tafel plots of different electrocatalysts. (d) HER polarization curves of PtCo/C NW before and after 1000 potential cycles.

was assessed by cycling between 0.6 and 1.1 V versus RHE in 0.1 M HClO_4 at a scan rate of 50 mV/s . Figure 4d shows the ORR polarization curves of the PtCo/C NW, before, after 5k and 10k potential cycles with negligible changes after cycling. It also maintained its initial ECSA (Figure S19) after ADT.

3.3. PEM Fuel Cell MEA Performance and Durability.

Motivated by the excellent performance of the PtCo/C NW catalyst system in the liquid half-cell tests, PEMFC practicability was accessed by analyzing both activity and durability in a single-cell MEA according to US DOE protocol.⁴⁵ The ADT protocol is designed to assess cathode electrocatalyst durability through successive cycles of surface oxidation and reduction causing accelerated catalyst degradation in a voltage range similar to the automotive drive cycle as suggested by the US DOE (see the Experimental Details section for details) (see Figure S20). The single-cell was operated at 80°C with fully humidified hydrogen and oxygen supplied into the anode and cathode, respectively, while maintaining a 0.5 bar back pressure on both electrodes. Metal loading was kept at $0.13 \text{ mg}/\text{cm}^2$ for both anode and cathode. Commercial Pt/C (19.4 wt % Pt, Tanaka Kikinzoku Kogyo (TKK), Japan) was used as an anode catalyst throughout all the measurements.

Figure 5a–c depicts the polarization curves for the various MEAs fabricated with the PtCo/C NW, PtCo/C NP, and Pt/C cathode electrocatalysts, respectively. At 0.8 V , the MEA with PtCo/C NW and PtCo/C NP as the cathode electrocatalysts delivered a beginning of life current densities of 285 and $175 \text{ mA}/\text{cm}^2$, respectively. These current densities are 103 and 25% higher than that of commercial Pt/C ($140 \text{ mA}/\text{cm}^2$), revealing the much-improved ORR kinetics on the PtCo/C NW. Specifically, the MAs at 0.8 V are, respectively, 2.19 , 1.35 , and $1.08 \text{ A}/\text{mg}_{\text{Pt}}$ for PtCo/C NW, PtCo/C NP, and Pt/C catalysts. The PtCo/C NW as a cathode catalyst reached a maximum power density of $1495 \text{ mW}/\text{cm}^2$ which is higher

than the PtCo/C NP catalyst ($1325 \text{ mW}/\text{cm}^2$) and the commercial Pt/C ($1295 \text{ mW}/\text{cm}^2$). We must mention that even though the MA of the PtCo NW is significantly higher than that of PtCo NP, the maximum power density of the NW is only slightly higher than the NP. This is because the NW system lacks the high ECSA required for high peak power performance due to the thick diameter of the NW. Despite the lower ECSA, the high MA and SA compensated this loss, and the large diameter of the NWs enhanced the stability of the catalyst as shown in Figure 5. This further shows that the observed higher MA of PtCo/C NW in the RDE test is reproducible in the MEA. After cycling the catalyst through the ADT protocol for 30k cycles, all three catalysts tested depicted a decrease in catalytic performance. As shown in Figure 5d, the peak power performance of the PtCo/C NW dropped by only 18% relative to the 38 and 64% peak power drop for the PtCo/C NP, and Pt/C, respectively, after 30k cycles.

This depicts the excellent durability of the PtCo/C NW MEA. It is also observed that the rate of degradation especially for the two alloys (PtCo/C NW and PtCo/C NP) as depicted in the polarization curves is significantly different. While the PtCo/C NW catalyst degradation rate drops steadily with successive periods of cycling, the PtCo/C NP catalyst consistently degrades at approximately the same rate during successive cycling. This observation demonstrates that the NWs develop immunity as they progress through the catalytic life cycle, whereas the NPs constantly degrade without any immunity. Post ADT TEM analysis and the corresponding selected-area FFT patterns indicates that the PtCo/C NW catalyst maintains its shape and crystallinity after the durability test, whereas the PtCo/C NP and Pt/C catalyst lose their crystallinity, as illustrated in Figure S21. We further analyzed the catalyst composition after MEA durability test with XPS and STEM–EDS. There was no XPS detectable cobalt for both PtCo/C NW and PtCo/C NP (Figures S22 and S23).

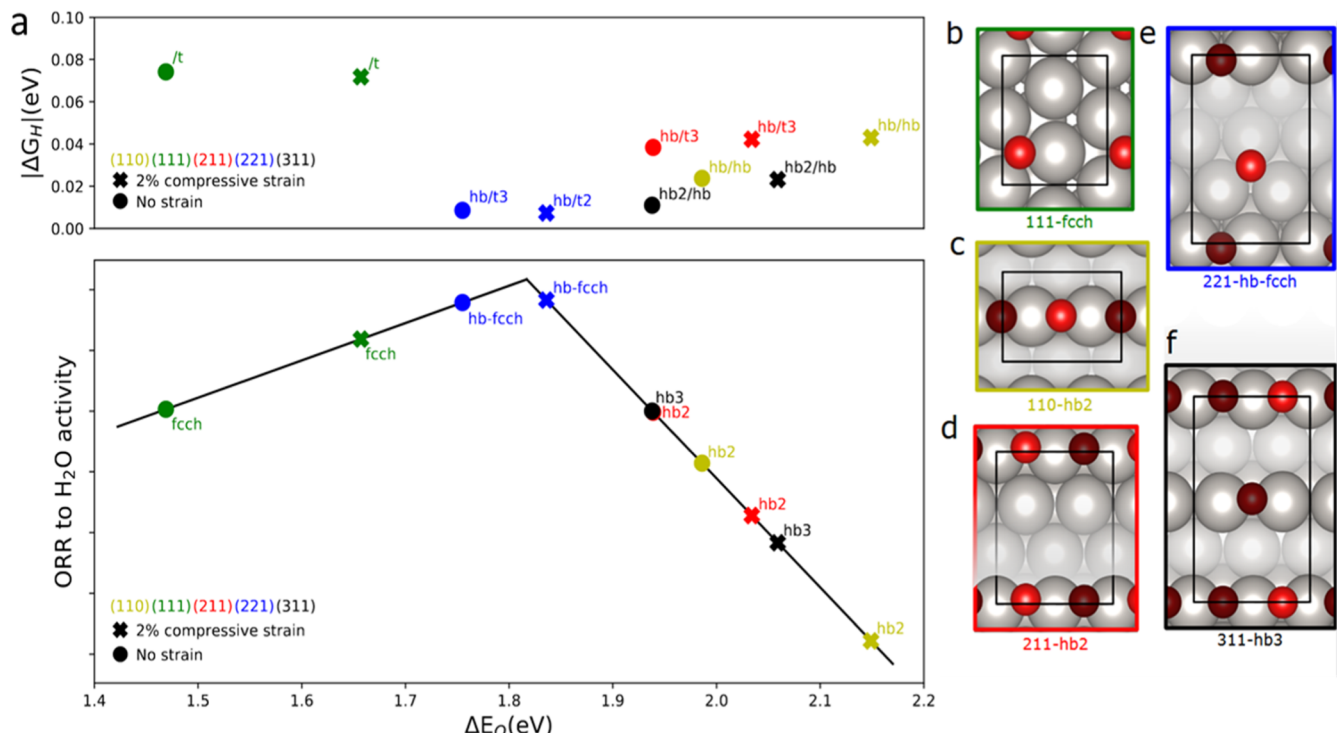


Figure 7. (a) HER activity estimated by the hydrogen adsorption free energy (upper panel) and ORR to H_2O activity (lower panel) based on activity estimate from ref 22. Both activity estimates are given as a function of the oxygen adsorption energy as a descriptor. Only the adsorption energies on the most stable adsorption sites for the (111), (110), (211), (221), and (311) facets are given with 50% oxygen coverage on the step-bridge site of all stepped surfaces due to the strong adsorption of oxygen atoms to the step-bridge site (b–f). The optimized geometries for the non-strained cases are depicted in (b–f) with the super cell highlighted by the dashed rectangle. Gray colored spheres indicate Pt atoms, light red for oxygen atoms which are given in the volcano plot in (a), and dark red for oxygen atoms which are fixed during the adsorption process.

This is because the concentration of the remaining cobalt in the spent catalyst layer is lower than the XPS detection limit due to the presence of high amount of ionomer (Nafion) as can be seen from the fluorine and carbon peaks of the XPS survey spectrum (Figures S22 and S23). Moreover, XPS is a surface sensitive technique with shallow sensing depth. STEM–EDS results on the other hand show that cobalt was still present after the ADT measurements (Figures S24 and S25). The final Co composition in the PtCo/C NW is 0.38. This corresponds to about 23% loss in alloying cobalt relative to the pristine sample. In comparison, the PtCo/C NP shows a final Co composition of 0.11 which is a significant 78% loss in initial alloying cobalt. These results further prove that our design technique slows down the rate of Co leaching from the catalyst.

3.4. Catalytic Activity and Durability for HER in Both Acidic and Alkaline Media. HER is the reaction occurring at the cathode of electrolyzers used to produce hydrogen through water splitting.⁴⁶ For the HER, all the catalysts were first evaluated by recording the linear sweep voltammetry (LSV) in N_2 -saturated 0.5 M H_2SO_4 . The polarization curve is an integral component to assess the hydrogen generation performance of an electrocatalyst. Figure S26 shows the polarization curves of Pt/C, PtCo/C NP, and PtCo/C NW with a scan rate of 10 mV/s. Though all the tested catalysts display a small overpotential \sim 20 mV to reach a current density of 10 mA/cm², both the PtCo/C NP and PtCo/C NW showed slightly enhanced performance relative to the commercial Pt/C. In order to approach industrial current densities and ensure the practicability of these catalysts for the

alkaline water electrolyzer, the HER performance was further evaluated in 1.0 M KOH by depositing the catalyst on nickel foam (NF) through dip coating. It is well known that the HER is two to three folds facile in acidic media as compared to alkaline media,⁴⁶ which explains why all the catalysts displayed slightly higher overpotential at a current density of 10 mA/cm² in 1.0 M KOH relative to 0.5 M H_2SO_4 . Moreover, in alkaline condition, a clear distinction in HER performance between the PtCo alloy and the commercial Pt was observed. Figure 6a shows the LSV polarization curves of Pt/C, PtCo/C NP, and PtCo/C NW with a scan rate of 10 mV/s in 1.0 M KOH, depicting the superior performance of the alloy system. The PtCo/C NW and PtCo/C NP required overpotentials of 32.7 and 34.6 mV, respectively (Figure 6b), while the commercial Pt/C required an overpotential of 45.7 mV to drive a current density of 10 mA/cm². To provide more insights into the HER kinetics of the electrocatalysts, the Tafel slopes were analyzed. As shown in Figure 6c, the PtCo/C NW exhibits the lowest Tafel slope of 33.9 mV/dec, which is slightly lower than that of the PtCo/C NP (38.2 mV/dec) and the commercial Pt/C (46 mV/dec), demonstrating the superior HER kinetics of PtCo/C NW. As a widely known fact, the HER consists of two major pathways (hydronium ion reduction and water reduction) which are further composed of three elementary reaction steps, that is, a primary discharge step (Volmer step, with a Tafel slope of 120 mV/dec), an electrochemical desorption step (Heyrovsky step, with a Tafel slope of 40 mV/dec) or a recombination step (Tafel step, with a Tafel slope of 30 mV/dec). As the rate-determining step (RDS) reflects the Tafel slope, the variation in Tafel slopes observed in the three

catalysts can be attributed to the change in the RDS in HER processes.⁴⁷ Based solely on the calculated Tafel slopes, it is found that the HER on both PtCo/C NP and Pt/C follow the Volmer–Heyrovsky mechanism, whereas the mechanism on PtCo/C NW is Volmer–Tafel.⁴⁶ The lower Tafel slope of both alloys (PtCo/C NP and NW) emphasizes the beneficial effects of cobalt alloying, whereas the different HER mechanistic pathways of the two alloys could be attributed to the high-index facets of the PtCo/C NW because the reaction mechanism strongly depends on the inherent surface chemistry and electronic structure of the catalyst.

By comparing the polarization curves before and after 1000 continuous CV cycles performed at a scan rate of 100 mV/s between +0.20 and −0.20 V versus RHE, the polarization curve after 1000 cycles almost overlays with the initial polarization curve of PtCo/C NW, reflecting the high durability of the PtCo/C NW. The practicability of the catalyst was also evaluated by subjecting it to the chronopotentiometry test for 12 h in 1.0 M KOH. As shown in Figure S27, the PtCo NW catalyst displays the most stable potential with the smallest degradation rate over the 12 h time interval.

Electrochemical impedance spectroscopy was used to confirm the lower charge transfer resistance of the alloy catalysts relative to commercial Pt/C (Figure S28). The Nyquist plots for commercial (Pt/C)/NF, (PtCo/C NP)/NF, and (PtCo/C NW)/NF with the exception of NF all display similar characteristics, that is, a depressed semi-circle in the high-frequency region. The depressed semi-circle is associated with the charge transfer at the catalyst/electrolyte interface. The lower the diameter of the semi-circle, the lower the charge transfer resistance at the interface. As clearly observed in the plot, the NF presents the largest diameter (almost out of range), followed by (Pt/C)/NF, (PtCo/C NW)/NF, and (PtCo/C NP)/NF. This result suggests that, at the same overpotential of 30 mV, the PtCo alloys present the fastest electron transfer in the reaction kinetics.

3.5. Theoretical Investigation of the Origin of ORR and HER Performance (DFT Calculation). To investigate the origin of the high ORR activity, we conducted DFT calculations, probing the oxygen adsorption free energies on a series of catalytic sites. The oxygen adsorption energy (E_O) is generally regarded a descriptor for ORR activity⁴⁸ and there exists an optimal value of E_O for which the ORR activity reaches its maximum. Starting with the Pt(111) facet, we found in accordance with previous literature that, the fcc hollow site exhibits the most stable oxygen binding (*O), 0.35 eV stronger relative to the optimum of the activity volcano (Figure 7, lower panel).⁴⁸

For the stepped facets, we evaluated the *O adsorption energy on all possible sites (Tables S2 and S3) and noticed a strong dominant adsorption on the bridge site of the step (high bridge “hb”). On the (211) surface step representing the intersection of two (111) terraces, the binding at the hb site is −0.73 eV relative to the optimum volcano, representing a rather strong adsorption. Interestingly, similar strong adsorption was also noticed on the other stepped surfaces (Figure 7, lower panel). It is known that on the (111) facet, oxygen coverages of ~10–20% occur at the applied voltages of ~0.9 V versus RHE⁴⁸ which is the applied potential in our study (Figure 4b). For stronger binding step sites, the expected coverage is thus much higher, as also shown by previous experimental studies.⁴⁹ We used the general Lang, Joyner, and

Somorjai notation to describe high-index facets, that is, $n(h_t k_t l_t) \times (h_s k_s l_s)$; t—terrace and s—step.²⁷ The general notation means n atomic width $n(h_t k_t l_t)$ of terraces, followed by monoatomic ($h_s k_s l_s$) steps. The calculated d -spacing shows that the PtCo/C NW with (221), (211), and (311) index facets was bounded by (110) and (111) atomic steps, while the PtCo/C NP was just terminated uniformly by (111) facets. This confirms that the PtCo/C NW catalyst exhibits many step sites, which results in a high oxygen coverage. In light of these results, we considered occupying 50% of the hb sites with oxygen seemed reasonable. Interestingly, similar strong adsorption was also noticed on the other stepped surfaces. With 50% oxygen coverage on the steps, enhanced activity was noted on the (110), (211), and (311) surfaces for the vacant hb sites. The less stable adsorption of oxygen on those hb sites compared to the (111) facets, suggests that the step sites are not completely covered, but instead the remaining empty sites can serve as highly active ORR centers. The resulting activity trend (211) > (110) > (111) is also in line with the experimental data under acidic conditions.⁴⁹ This increases the confidence in the rough estimate of the steady-state coverage. In contrast, on the (221) surface including long terraces, adsorption happens preferably on the fcc hollow sites of the terraces. The shorter Pt–Pt distances corresponding to compressive strain on the (221) terrace relative to the (111) facet destabilizes *O, thereby weakening the adsorption and thus boosting the ORR activity.⁵⁰

To investigate the effect of Co alloying, we applied compressive strain to the super cell in the x – y direction. This procedure follows the results of previous works that Co atoms are only present in the sub-surface layers and the ligand effect on the adsorption energies is minimal compared to the strain effect.⁹ From our DFT calculations, an fcc CoPt crystal exhibits a compressively strained bulk crystal relative to fcc Pt by −4.2%. However, in our experiments, we found the Co-lean-Pt shell to be around 2 nm thick (Figure 3), corresponding to roughly 8 layers in the (111) direction. This drastically reduces the strain of the surface layer. We thus considered a reduced value of −2% to qualitatively estimate the change in adsorption energies.^{9,51} As seen from Figure 7, binding to the (111) surface is significantly weakened by the presence of Co, thereby activating the fcc hollow sites for ORR. Oxygen adsorption on the 50% oxygen-hb covered (211), (311), and (110) surface also becomes weaker, but due to the location of these sites on the weak-binding leg, this essentially leads to a deactivation for ORR. The adsorption on the fcc hollow site of 50% oxygen-hb covered (221) surface, in contrast, due to its location on the strong binding leg, moves toward the top of the volcano amid less strong binding of *O. From these theoretical results, we thus expect the increased activity of our catalyst to originate from fcc hollow sites of the (221) facet. Their high activity owes to the favorable compressive strain emanating from both the nature of the high-index facet and the intercalation of Co in the sub-surface layers, as well as the extended terraces that avoid interaction with the covered step sites.

Finally, we also evaluated the activity of the different surface facets for HER (Figure 7, upper panel) by calculating the hydrogen adsorption free energy. An adsorption energy of 0 is usually considered as optimal for a high HER rate.^{S2–S4} By investigating the different facets, we found the fcc hollow sites of the (221) surface to be also most active for HER compared to the other facets. Here, the oxygen coverage on the bridge

sites destabilizes the adsorbed hydrogen slightly in favor of a higher HER activity (Table S4 in the [Supporting Information](#)). In contrast to the oxygen coverage, Co-doping was, however, found for all surfaces to be relatively ineffective in tuning the hydrogen adsorption energy, which is why we expect the same HER activity trends for pure Pt electrodes.

4. CONCLUSIONS

We have successfully prepared a highly durable and active PtCo alloy with multiple structural and compositional advantages via a facile wet-chemical route. The alloy catalyst displayed excellent performance for both ORR and HER. DFT calculations revealed that the enhanced ORR performance originates from the presence of a Pt(221) high-index facet whose dominant presence in our catalyst was confirmed by HR-TEM. The (111) terraces of the (221) facet are strained enough by both the presence of sub-surface Co and the nature of the high-index facet to yield excellent catalytic activity of the fcc hollow sites and extended enough to avoid deactivation by interacting with the oxygen coverage on the step sites. The large NW diameters contributed immensely to the catalyst durability, and the highly active facets compensated for the low ECSA. Moreover, contrary to reports on the instability often associated with high alloying element content typical of Pt_1M_1 alloy structures, we observe that the Pt-rich shell and the stable intermetallic Pt–Co arrangement in the core enhance the stability of the catalyst while preventing the dissolution of the alloying element (Co). The 1D structure provided higher contact area with the carbon support which prevented detachment from the carbon support and hence required no protection during phase transformation to the intermetallic structure via thermal annealing making the NWs thermally stable. Furthermore, the practicability of this catalyst was demonstrated by evaluating the catalyst activity and durability in a single-cell PEMFC MEA. The alloy NW catalyst (PtCo/C NW) delivered the best peak power performance relative to the PtCo/C NP and Pt/C along with the best durability. This work represents a significant step ahead in the systematic design of Pt-based fuel cell catalyst by utilizing strain control using additive metal embedded core–shell technology, nano-structure design, and coverage control. We think that these new insights demonstrated by the development of a cost-effective, active, and durable PtCo NW fuel cell catalyst will have a significant impact on the development of industrially competitive fuel cell systems.

■ ASSOCIATED CONTENT

§ Supporting Information

The Supporting Information is available free of charge at <https://pubs.acs.org/doi/10.1021/acsami.2c00398>.

Experimental details, computational methods, additional physicochemical and electrochemical characterizations, DFT calculation results, “POSCAR” geometry file, TEM images, XRD spectra, HR-TEM images, STEM images, XPS spectra, high-resolution Co 2p XPS profiles, CV results, DOE accelerated degradation test, EDS analysis, HER curves, EIS spectra, ORR mass activity, adsorption sites and resulting adsorption energies, and all computational input files and results have been uploaded to the catalysis-hub database and are available online at <https://www.catalysishub.org/publications/TettehCompressively2022> (PDF)

■ AUTHOR INFORMATION

Corresponding Authors

Stefan Ringe – Department of Energy Science and Engineering, Daegu Gyeongbuk Institute of Science & Technology (DGIST), Daegu 42988, Republic of Korea; Department of Chemistry, Korea University, Seoul 02841, Republic of Korea; orcid.org/0000-0002-7804-1406; Email: sringe@korea.ac.kr

Jong-Sung Yu – Department of Energy Science and Engineering, Daegu Gyeongbuk Institute of Science & Technology (DGIST), Daegu 42988, Republic of Korea; orcid.org/0000-0002-8805-012X; Email: jsyu@dgist.ac.kr

Authors

Emmanuel Batsa Tetteh – Department of Energy Science and Engineering, Daegu Gyeongbuk Institute of Science & Technology (DGIST), Daegu 42988, Republic of Korea; Analytical Chemistry—Center for Electrochemical Sciences (CES), Faculty for Chemistry and Biochemistry, Ruhr University Bochum, Bochum 44780, Germany

Caleb Gyan-Barimah – Department of Energy Science and Engineering, Daegu Gyeongbuk Institute of Science & Technology (DGIST), Daegu 42988, Republic of Korea

Ha-Young Lee – Department of Energy Science and Engineering, Daegu Gyeongbuk Institute of Science & Technology (DGIST), Daegu 42988, Republic of Korea

Tong-Hyun Kang – Department of Energy Science and Engineering, Daegu Gyeongbuk Institute of Science & Technology (DGIST), Daegu 42988, Republic of Korea

Seonghyeon Kang – Department of Energy Science and Engineering, Daegu Gyeongbuk Institute of Science & Technology (DGIST), Daegu 42988, Republic of Korea

Complete contact information is available at:
<https://pubs.acs.org/10.1021/acsami.2c00398>

Author Contributions

[¶]E.B.T, C. G.-B., and H.-Y.L. contributed equally.

Notes

The authors declare no competing financial interest.

■ ACKNOWLEDGMENTS

This work was generously supported by National Research Foundation (NRF-2019R1A2C2086770), (NRF-2019K2A9A1A06100164), and (NRF-2021R1C1C1008776) funded by the Korea Ministry of Science, ICT & Future Planning, Authors would also like to thank the Korean Basic Science Institute at Jeonju (SEM and HRTEM analysis), Daejeon (TEM analysis), and the CCRF at DGIST. S.R. thanks Seoin Back for insightful discussions.

■ ABBREVIATIONSPARA

NW, nanowire
NP, nanoparticle
1-D, one dimensional
fct, face centered tetragonal

■ REFERENCES

- (1) U.S. Energy Information Administration. *International Energy Outlook*, 2016.

- (2) Yoshida, T.; Kojima, K. Toyota MIRAI Fuel Cell Vehicle and Progress Toward a Future Hydrogen Society. *Interface* **2015**, *24*, 45–49.
- (3) Fang, B.; Chaudhari, N. K.; Kim, M.-S.; Kim, J. H.; Yu, J.-S. Homogeneous Deposition of Platinum Nanoparticles on Carbon Black for Proton Exchange Membrane Fuel Cell. *J. Am. Chem. Soc.* **2009**, *131*, 15330–15338.
- (4) Kodama, K.; Nagai, T.; Kuwaki, A.; Jinnouchi, R.; Morimoto, Y. Challenges in Applying Highly Active Pt-Based Nanostructured Catalysts for Oxygen Reduction Reactions to Fuel Cell Vehicles. *Nat. Nanotechnol.* **2021**, *16*, 140–147.
- (5) Tetteh, E. B.; Löffler, T.; Tarnev, T.; Quast, T.; Wilde, P.; Aiyappa, H. B.; Schumacher, S.; Andronescu, C.; Tilley, R. D.; Chen, X.; Schuhmann, W. Calibrating SECCM Measurements by Means of a Nanoelectrode Ruler: The Intrinsic Oxygen Reduction Activity of PtNi Catalyst Nanoparticles. *Nano Res.* **2021**, *15*, 1564–1569.
- (6) Chen, Q.; Cao, Z.; Du, G.; Kuang, Q.; Huang, J.; Xie, Z.; Zheng, L. Excavated Octahedral Pt-Co Alloy Nanocrystals Built with Ultrathin Nanosheets as Superior Multifunctional Electrocatalysts for Energy Conversion Applications. *Nano Energy* **2017**, *39*, 582–589.
- (7) Wang, L.; Holewinski, A.; Wang, C. Prospects of Platinum-Based Nanostructures for the Electrocatalytic Reduction of Oxygen. *ACS Catal.* **2018**, *8*, 9388–9398.
- (8) Chong, L.; Wen, J.; Kubal, J.; Sen, F. G.; Zou, J.; Greeley, J.; Chan, M.; Barkholtz, H.; Ding, W.; Liu, D.-J. Ultralow-Loading Platinum-Cobalt Fuel Cell Catalysts Derived from Imidazolate Frameworks. *Science* **2018**, *362*, 1276–1281.
- (9) Bu, L.; Guo, S.; Zhang, X.; Shen, X.; Su, D.; Lu, G.; Zhu, X.; Yao, J.; Guo, J.; Huang, X. Surface Engineering of Hierarchical Platinum-Cobalt Nanowires for Efficient Electrocatalysis. *Nat. Commun.* **2016**, *7*, 11850.
- (10) Stamenkovic, V. R.; Mun, B. S.; Arenz, M.; Mayrhofer, K. J. J.; Lucas, C. A.; Wang, G.; Ross, P. N.; Markovic, N. M. Trends in Electrocatalysis on Extended and Nanoscale Pt-Bimetallic Alloy Surfaces. *Nat. Mater.* **2007**, *6*, 241–247.
- (11) Tran, T.-N.; Lee, H.-Y.; Park, J.-D.; Kang, T.-H.; Lee, B.-J.; Yu, J.-S. Synergistic CoN-Decorated Pt Catalyst on Two-Dimensional Porous Co-N-Doped Carbon Nanosheet for Enhanced Oxygen Reduction Activity and Durability. *ACS Appl. Energy Mater.* **2020**, *3*, 6310–6322.
- (12) Zhu, X.; Huang, L.; Wei, M.; Tsiaikaras, P.; Shen, P. K. Highly Stable Pt-Co Nanodendrite in Nanoframe with Pt Skin Structured Catalyst for Oxygen Reduction Electrocatalysis. *Appl. Catal. B Environ.* **2021**, *281*, 119460.
- (13) Sievers, G. W.; Jensen, A. W.; Quinson, J.; Zana, A.; Bizzotto, F.; Oezaslan, M.; Dworzak, A.; Kirkensgaard, J. J. K.; Smitshuyzen, T. E. L.; Kadkhodazadeh, S.; Juelsholte, M.; Jensen, K. M. Ø.; Anklam, K.; Wan, H.; Schäfer, J.; Cépe, K.; Escudero-Escribano, M.; Rossmeisl, J.; Quade, A.; Brüser, V.; Arenz, M. Self-Supported Pt–CoO Networks Combining High Specific Activity with High Surface Area for Oxygen Reduction. *Nat. Mater.* **2021**, *20*, 208–213.
- (14) Xie, M.; Lyu, Z.; Chen, R.; Shen, M.; Cao, Z.; Xia, Y. Pt-Co@Pt Octahedral Nanocrystals: Enhancing Their Activity and Durability toward Oxygen Reduction with an Intermetallic Core and an Ultrathin Shell. *J. Am. Chem. Soc.* **2021**, *143*, 8509–8518.
- (15) Zhang, S.; Zhang, X.; Jiang, G.; Zhu, H.; Guo, S.; Su, D.; Lu, G.; Sun, S. Tuning Nanoparticle Structure and Surface Strain for Catalysis Optimization. *J. Am. Chem. Soc.* **2014**, *136*, 7734–7739.
- (16) Choi, D. S.; Robertson, A. W.; Warner, J. H.; Kim, S. O.; Kim, H. Low-Temperature Chemical Vapor Deposition Synthesis of Pt-Co Alloyed Nanoparticles with Enhanced Oxygen Reduction Reaction Catalysis. *Adv. Mater.* **2016**, *28*, 7115–7122.
- (17) Luo, M.; Guo, S. Strain-Controlled Electrocatalysis on Multimetallic Nanomaterials. *Nat. Rev. Mater.* **2017**, *2*, 17059.
- (18) Debe, M. K. Electrocatalyst Approaches and Challenges for Automotive Fuel Cells. *Nature* **2012**, *486*, 43–51.
- (19) Kulkarni, A.; Siahrostami, S.; Patel, A.; Nørskov, J. K. Understanding Catalytic Activity Trends in the Oxygen Reduction Reaction. *Chem. Rev.* **2018**, *118*, 2302–2312.
- (20) Xu, R.; Du, L.; Adekoya, D.; Zhang, G.; Zhang, S.; Sun, S.; Lei, Y. Well-Defined Nanostructures for Electrochemical Energy Conversion and Storage. *Adv. Energy Mater.* **2020**, *11*, 2001537.
- (21) Li, D.; Wang, C.; Strmenik, D. S.; Tripkovic, D. V.; Sun, X.; Kang, Y.; Chi, M.; Snyder, J. D.; van der Vliet, D.; Tsai, Y.; Stamenkovic, V. R.; Sun, S.; Markovic, N. M. Functional Links between Pt Single Crystal Morphology and Nanoparticles with Different Size and Shape: The Oxygen Reduction Reaction Case. *Energy Environ. Sci.* **2014**, *7*, 4061–4069.
- (22) Tian, N.; Zhou, Z.-Y.; Sun, S.-G. Platinum Metal Catalysts of High-Index Surfaces: From Single-Crystal Planes to Electrochemically Shape-Controlled Nanoparticles. *J. Phys. Chem. C* **2008**, *112*, 19801–19817.
- (23) Quan, Z.; Wang, Y.; Fang, J. High-Index Faceted Noble Metal Nanocrystals. *Acc. Chem. Res.* **2013**, *46*, 191–202.
- (24) Singh, K.; Tetteh, E. B.; Lee, H.-Y.; Kang, T.-H.; Yu, J.-S. Tailor-Made Pt Catalysts with Improved Oxygen Reduction Reaction Stability/Durability. *ACS Catal.* **2019**, *9*, 8622–8645.
- (25) Luo, M.; Sun, Y.; Wang, L.; Guo, S. Tuning Multimetallic Ordered Intermetallic Nanocrystals for Efficient Energy Electrocatalysis. *Adv. Energy Mater.* **2017**, *7*, 1602073.
- (26) Wang, C.; Spendelow, J. S. Recent Developments in Pt–Co Catalysts for Proton-Exchange Membrane Fuel Cells. *Current Opinion in Electrochemistry*; Elsevier B.V., August 1, 2021.
- (27) Huang, X.; Zhao, Z.; Chen, Y.; Zhu, E.; Li, M.; Duan, X.; Huang, Y. A Rational Design of Carbon-Supported Dispersive Pt-Based Octahedra as Efficient Oxygen Reduction Reaction Catalysts. *Energy Environ. Sci.* **2014**, *7*, 2957–2962.
- (28) Zhang, C.; Shen, X.; Pan, Y.; Peng, Z. A Review of Pt-Based Electrocatalysts for Oxygen Reduction Reaction. *Front. Energy* **2017**, *11*, 268–285.
- (29) Li, L.; Hu, L.; Li, J.; Wei, Z. Enhanced Stability of Pt Nanoparticle Electrocatalysts for Fuel Cells. *Nano Res.* **2015**, *8*, 418–440.
- (30) Lv, H.; Mu, S.; Cheng, N.; Pan, M. Nano-Silicon Carbide Supported Catalysts for PEM Fuel Cells with High Electrochemical Stability and Improved Performance by Addition of Carbon. *Appl. Catal. B Environ.* **2010**, *100*, 190–196.
- (31) Xiao, W.; Lei, W.; Gong, M.; Xin, H. L.; Wang, D. Recent Advances of Structurally Ordered Intermetallic Nanoparticles for Electrocatalysis. *ACS Catal.* **2018**, *8*, 3237–3256.
- (32) Wang, T.; Liang, J.; Zhao, Z.; Li, S.; Lu, G.; Xia, Z.; Wang, C.; Luo, J.; Han, J.; Ma, C.; Huang, Y.; Li, Q. Sub-6 nm Fully Ordered L_1 -Pt–Ni–Co Nanoparticles Enhance Oxygen Reduction via Co Doping Induced Ferromagnetism Enhancement and Optimized Surface Strain. *Adv. Energy Mater.* **2019**, *9*, 1803771.
- (33) Gong, M.; Xiao, D.; Deng, Z.; Zhang, R.; Xia, W.; Zhao, T.; Liu, X.; Shen, T.; Hu, Y.; Lu, Y.; Zhao, X.; Xin, H.; Wang, D. Structure Evolution of PtCu Nanoframes from Disordered to Ordered for the Oxygen Reduction Reaction. *Appl. Catal. B Environ.* **2021**, *282*, 119617.
- (34) Li, J.; Sharma, S.; Liu, X.; Pan, Y.-T.; Spendelow, J. S.; Chi, M.; Jia, Y.; Zhang, P.; Cullen, D. A.; Xi, Z.; Lin, H.; Yin, Z.; Shen, B.; Muzzio, M.; Yu, C.; Kim, Y. S.; Peterson, A. A.; More, K. L.; Zhu, H.; Sun, S. Hard-Magnet L_1 -CoPt Nanoparticles Advance Fuel Cell Catalysis. *Joule* **2019**, *3*, 124–135.
- (35) Wang, D.; Xin, H. L.; Hovden, R.; Wang, H.; Yu, Y.; Muller, D. A.; DiSalvo, F. J.; Abruna, H. D. Structurally ordered intermetallic platinum-cobalt core-shell nanoparticles with enhanced activity and stability as oxygen reduction electrocatalysts. *Nat. Mater.* **2013**, *12*, 81–87.
- (36) Bu, L.; Zhang, N.; Guo, S.; Zhang, X.; Li, J.; Yao, J.; Wu, T.; Lu, G.; Ma, J.-Y.; Su, D.; Huang, X. Biaxially Strained PtPb/Pt Core/Shell Nanoplate Boosts Oxygen Reduction Catalysis. *Science* **2016**, *354*, 1410–1414.
- (37) Tetteh, E. B.; Lee, H.-Y.; Shin, C.-H.; Kim, S.-h.; Ham, H. C.; Tran, T.-N.; Jang, J.-H.; Yoo, S. J.; Yu, J.-S. New PtMg Alloy with Durable Electrocatalytic Performance for Oxygen Reduction Reaction

- in Proton Exchange Membrane Fuel Cell. *ACS Energy Lett.* **2020**, *5*, 1601–1609.
- (38) Zhao, Z.; Dubau, L.; Maillard, F. Evidences of the Migration of Pt Crystallites on High Surface Area Carbon Supports in the Presence of Reducing Molecules. *J. Power Sources* **2012**, *217*, 449–458.
- (39) Li, B.; Higgins, D. C.; Xiao, Q.; Yang, D.; Zhng, C.; Cai, M.; Chen, Z.; Ma, J. The Durability of Carbon Supported Pt Nanowire as Novel Cathode Catalyst for a 1.5 kW PEMFC Stack. *Appl. Catal. B Environ.* **2015**, *162*, 133–140.
- (40) Bu, L.; Feng, Y.; Yao, J.; Guo, S.; Guo, J.; Huang, X. Facet and Dimensionality Control of Pt Nanostructures for Efficient Oxygen Reduction and Methanol Oxidation Electrocatalysts. *Nano Res.* **2016**, *9*, 2811–2821.
- (41) Zhang, N.; Bu, L.; Guo, S.; Guo, J.; Huang, X. Screw Thread-Like Platinum-Copper Nanowires Bounded with High-Index Facets for Efficient Electrocatalysis. *Nano Lett.* **2016**, *16*, 5037–5043.
- (42) Bu, L.; Ding, J.; Guo, S.; Zhang, X.; Su, D.; Zhu, X.; Yao, J.; Guo, J.; Lu, G.; Huang, X. A General Method for Multimetallic Platinum Alloy Nanowires as Highly Active and Stable Oxygen Reduction Catalysts. *Adv. Mater.* **2015**, *27*, 7204–7212.
- (43) Hammer, B.; Morikawa, Y.; Nørskov, J. K. CO Chemisorption at Metal Surfaces and Overlayers. *Phys. Rev. Lett.* **1996**, *76*, 2141–2144.
- (44) Department of Energy. DOE Technical Targets for Polymer Electrolyte Membrane Fuel Cell Components. <https://www.energy.gov/eere/fuelcells/doe-technical-targets-polymer-electrolyte-membrane-fuel-cell-components> (accessed September 2019).
- (45) Department of Energy (DOE). *Electrocatalyst Durability Protocols for PEM Fuel Cells*; US Department of Energy (DOE), 2016.
- (46) Mahmood, N.; Yao, Y.; Zhang, J.-W.; Pan, L.; Zhang, X.; Zou, J.-J. Electrocatalysts for Hydrogen Evolution in Alkaline Electrolytes: Mechanisms, Challenges, and Prospective Solutions. *Adv. Sci.* **2018**, *5*, 1700464.
- (47) Shinagawa, T.; Garcia-Esparza, A. T.; Takanabe, K. Insight on Tafel Slopes from a Microkinetic Analysis of Aqueous Electrocatalysis for Energy Conversion. *Sci. Rep.* **2015**, *5*, 13801.
- (48) Nørskov, J. K.; Rossmeisl, J.; Logadottir, A.; Lindqvist, L.; Kitchin, J. R.; Bligaard, T.; Jónsson, H. Origin of the Overpotential for Oxygen Reduction at a Fuel-Cell Cathode. *J. Phys. Chem. B* **2004**, *108*, 17886–17892.
- (49) Gómez-Marín, A. M.; Rizo, R.; Feliu, J. M. Oxygen Reduction Reaction at Pt Single Crystals: A Critical Overview. *Catal. Sci. Technol.* **2014**, *4*, 1685.
- (50) Tian, X.; Zhao, X.; Su, Y.-Q.; Wang, L.; Wang, H.; Dang, D.; Chi, B.; Liu, H.; Hensen, E. J. M.; Lou, X. W.; Xia, B. Y. Engineering Bunched Pt-Ni Alloy Nanocages for Efficient Oxygen Reduction in Practical Fuel Cells. *Science* **2019**, *366*, 850–856.
- (51) Kattel, S.; Wang, G. Beneficial Compressive Strain for Oxygen Reduction Reaction on Pt (111) Surface. *J. Chem. Phys.* **2014**, *141*, 124713.
- (52) Quaino, P.; Juarez, F.; Santos, E.; Schmickler, W. Volcano Plots in Hydrogen Electrocatalysis—Uses and Abuses. *Beilstein J. Nanotechnol.* **2014**, *5*, 846–854.
- (53) Seh, Z. W.; Kibsgaard, J.; Dickens, C. F.; Chorkendorff, I.; Nørskov, J. K.; Jaramillo, T. F. Combining Theory and Experiment in Electrocatalysis: Insights into Materials Design. *Science* **2017**, *355*, No. eaad4998.
- (54) Kibsgaard, J.; Tsai, C.; Chan, K.; Benck, J. D.; Nørskov, J. K.; Abild-Pedersen, F.; Jaramillo, T. F. Designing an Improved Transition Metal Phosphide Catalyst for Hydrogen Evolution Using Experimental and Theoretical Trends. *Energy Environ. Sci.* **2015**, *8*, 3022–3029.



CAS BIOFINDER DISCOVERY PLATFORM™

CAS BIOFINDER HELPS YOU FIND YOUR NEXT BREAKTHROUGH FASTER

Navigate pathways, targets, and diseases with precision

Explore CAS BioFinder

